*ISSN 1392–1207. MECHANIKA. 2023 Volume 29(1): 34–41*

# Transient Numerical Simulation of a Large-Sized Cement-Mill Fan for Performance Prediction

**Aissa AMOUR*, Noureddine MENASRI****
**Laboratory of Materials and Structural Mechanics, University of M'sila, B.P 1084 RP 2800 M'sila, Algeria, E-mail: aissa.amour@univ-msila.dz*
***Laboratory of Materials and Structural Mechanics, University of M'sila, Algeria, E-mail: Noureddine.Menasri@univ-msila.dz*
crossref http://dx.doi.org/10.5755/j02.mech.32170

## 1. Introduction

Many engineering applications and industries use centrifugal fans for various purposes. Among these key industries are the cement production plants, which require several industrial processes that fans are designed precisely for certain tasks. Cement-mill fan (FN-280), is an induced draft fan employed to generate a negative pressure air flow to ensure the good work of the dust abatement in a bag-filter housing as part of the emission process. This process gives rise to an undesirable circumstance when the cement particles are carried with the gas with a high load of about 30mg/Nm$^3$. The velocity of these dragged solid particles inside the centrifugal fan is sufficiently high to ensure that their impact on the stationary and rotating parts of the fan contributes to a loss of material, which over time this damage constitutes a challenging factor in terms of service-life operation of the fan. While experimental investigation of the erosion process in turbomachinery applications is difficult and costly, a numerical approach may provide an alternative. Regarding this fact, in order to track the erodent particles and have an in-depth insight into the erosion pattern by means of a numerical approach, it is crucial to accurately predict the 3D flow field to capture the peculiar flow physics within the centrifugal fan. However, the flow field in the fan is turbulent, characterized by a high Reynolds number with inevitable flow separation. Therefore, making the prediction of the flow field in the fan using computational methods a challenging task.

Assuming that the flow-field within the centrifugal fan is solved, it is possible to track the solid particles trajectory to model the erosion behavior. Cardillo L. et al. [1, 2] studied an industrial centrifugal fan installed in a cement production plant for erosion prediction, unsteady simulation was carried out at the peak pressure using the open-source solver OpenFOAM. Aldi N. et al. [3] studied the erosion behavior of a large-sized centrifugal fan, unsteady simulation was also employed by means of the commercial CFD code ANSYS CFX to take into account the effects of the flow unsteadiness in erosion prediction. Zhang J. et al.[4] tested a bionic blade configuration to minimize erosion, however they performed a steady state simulation. Song X. et al. [5] simulated the erosion pattern of a double suction pump at different flow rates with a discrete phase model (DPM) for solid particles and Eulerian approach for liquid phase. The trajectory of the erodent particles at different time instants of the simulation was taken into account in the Eulerian-Lagrangian approach, where the continuous phase is solved first , and the solid particles are treated as discrete elements [6, 7]. Computational fluid dynamic and the discrete element method (DEM) was also combined to simulate erosion in centrifugal pumps where the particle motion is modelled using the DEM then coupled with CFD in the fluid domain [8, 9].

Besides erosion prediction studies, many works focused on modelling turbomachines for performance enhancement and flow unsteadiness analysis also have been conducted. Ballesteros-Tajadura R. et al. [10] performed a 2D and a 3D unsteady simulation to obtain pressure fluctuation at the volute walls of an industrial centrifugal fan using k-$\varepsilon$ turbulence model, the unsteady numerical results agreed well with experiment for flow rates equal to and higher than the design operating point. Pritz B. et al. [11] studied the unsteadiness of the flow through a centrifugal fan, two turbulence models namely scale adaptive simulation (SAS-SST) and shear stress transport (SST) have been considered and compared in the study. Delayed detached eddy simulation was employed to study the evolution of the unsteady flow structure in turbomachinery [12–14]. The impact of the unsteady internal flow field induced by the relative motion of the rotating blade with the volute on the aeroacoustics behavior of centrifugal fans was investigated using CFD [15, 16].The influence of the pump geometry parameters, such as the blade outlet angle and the clearance between the impeller and its volute on the pump performance was investigated by means of numerical approach have been also conducted [17, 18].

Based on the discussion above, an accurate prediction of the flow field within the centrifugal fan constitutes the first step to be considered to model the erosion phenomenon numerically. Regarding this fact, in the present study, an unsteady numerical simulation of the three-dimensional flow field in a large-sized cement-mill fan installed in a cement plant is carried out to predict the performance of the fan. The unsteadiness in the flow field was accounted for by using the sliding mesh technique based on the SST *K-ω* turbulence model. computational results under different operating conditions were compared with the experimental data to validate the modelling approach effectiveness. Both time-averaged and instantaneous flow field were analyzed to provide an insight into the unsteadiness of the flow induced by the interaction of the impeller and the casing.

## 2. Description of the centrifugal fan

The studied fan is a large sized single inlet centrifugal fan operating in a cement plant. The fan impeller consists of 16 backward curved blades running at a rotational

speed of $N$ = 985 rpm. The reference velocity pressure ($p_{ref}$) based on the impeller tip speed $U_2$, is equal to 5459.04 Pa. The corresponding rotational frequency and impeller period are defined as $RF = N/60$ = 16.41 Hz and $T=1/RF$ = = 0.060913s respectively. The CAD model of the centrifugal fan was performed using SOLIDWORKS.A Coordinate measuring machine (CMM) was used as a reverse engineering tool for 3D scanning and the commercial software (Geomagic Design X) for point cloud processing and CAD modelling of the impeller blade. The aerodynamic performance of the studied fan was experimentally derived in accordance with the industrial fan testing standard ISO 5801 requirements [19]. The computational domain of the centrifugal fan was extracted using SpaceClaim and divided into three parts, namely the inlet cone, the rotating impeller, and the casing. The main design parameters of the fan are summarized in Table 1. Fig. 1 shows the whole computational domain of the fan where the origin was set at the center of the hub, the geometrical profile, and the blade alignment in the workspace are presented in Fig. 2.

Table 1

Main parameters of the centrifugal fan

| Main parameters | Values |
|---|---|
| Impeller outlet diameter $D_2$ | 2240 mm |
| Impeller inlet diameter $D_1$ | 1190 mm |
| Volute width | 900 mm |
| Impeller blade count | 16 |
| Blade thickness | 8 mm |
| Rotational speed, $N$ | 985 rpm |
| Impeller tip speed, $U_2$ | 115.46 m/s |
| Impeller outlet blade span | 280 mm |
| Impeller-tongue gap | 110 mm |
| $Q_d$ (design flow rate) | 53.9 $m^3/s$ |
| $\Delta H_d$ (design Total pressure rise) | 6148 Pa |

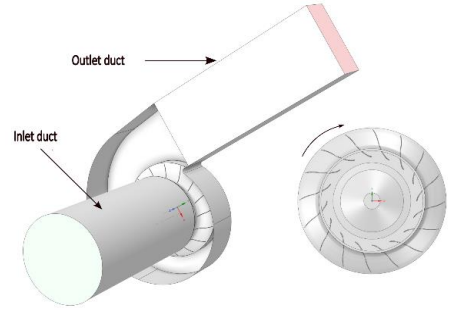


Fig. 1 General view of the computational domain

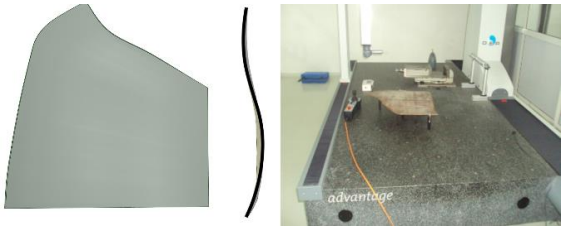

a b

Fig. 2 Fan blade geometry: a) the blade CAD model; b) the workspace for 3D scanning

## 3. Numerical modelling

### 3.1. Simulation approach

In turbomachine simulation, the rotating impeller involves mesh motion which makes the simulation inherently unsteady.in such a case, the unsteady Navier-Stokes equations are solved at every time step, therefore it requires more computational resources. An Alternative approach consists of transforming the equations of motion in the inertial frame from unsteady to steady with respect to the moving reference frame, this is done by adding the Coriolis and centripetal acceleration terms in the momentum equations. By transforming the momentum equations, a common approach referred to as single reference frame (SRF) can be used, where all the computational domain is solved in a single moving reference frame. With such an approach, one may model only a single blade passage with periodic boundary conditions. Therefore, the computational effort will be overly reduced. However, when considering modelling centrifugal fans, the geometry does not meet the SRF approach requirements [20] and consequently, the full rotor of the Centrifugal fan must be considered and the whole computational domain must be divided into multiple zones separated by interfaces to account for the coupling between rotating and stationary domain. This approach is referred to multiple reference frame (MRF) or the (frozen-rotor) approach. this approach has been widely adopted within the industrial fan community as it is an alternative setting to perform turbomachinery simulation with reduced time and effort.

Although the Frozen Rotor is an effective way to simulate rotating devices, Adding Coriolis and centripetal terms to the momentum equations in the rotating frame of reference constitutes an approximation of the flow field physics which may limit the accuracy of the numerical results [21]. To accurately capture the flow instability and its related phenomena, it's necessary to hold out a three-dimensional numerical simulation of the unsteady flow field in the whole domain of the centrifugal fan employing a sliding mesh technique within which the impeller domain moves physically relative to the stationary parts. consequently, the required computational effort is increased compared to (MRF). According to the discussion above, the modelling approach during this present paper follows two steps, A steady state simulation based on RANS using the MRF approach is first carried out, then the converged solution obtained is used as an initial solution for the unsteady simulation using the sliding mesh technique.

### 3.2. Mathematical model formulation

The computational domain of the centrifugal fan consists of two stationary fluid domains namely the inlet suction and the volute. The impeller domain was set to be rotating at a speed of 985 (rpm). The turbulent incompressible flow is governed by the Reynolds-averaged Navier–Stokes (RANS) Equations that read as follows:

$$\frac{\partial \overline{u_k}}{\partial x_k} = 0, \tag{1}$$

$$\frac{\partial \overline{u_i}}{\partial t} + \overline{u_k}\frac{\partial \overline{u_i}}{\partial x_k} = -\frac{1}{\rho}\frac{\partial \overline{p}}{\partial x_i} + \nu\frac{\partial \overline{u_i}}{\partial x_j \partial x_j} - \frac{\partial}{\partial x_k}\left(\overline{u_i' u_k'}\right), \tag{2}$$

where: $\overline{u_i}$ is the mean velocity component; $\overline{p}$ is the mean pressure; $\nu$ and $\rho$ are the kinematic viscosity and density of the fluid. the Reynolds-averaging process results in the additional term in parentheses known as the Reynolds stress.

The eddy-viscosity turbulence model namely the SST *k-ω* chosen in this study follows the Boussinesq's hypothesis to model the Reynolds stresses and is given as follows:

$$\overline{u_i' u_j'} = \frac{2}{3} k \delta_{ij} - \nu_t \left( \frac{\partial \overline{u_i}}{\partial x_j} + \frac{\partial \overline{u_j}}{\partial x_i} \right), \quad (3)$$

The model combines both the $k-\varepsilon$ and $k-\omega$ models, where the former solves the equation for the dissipation rate $\varepsilon$ of turbulent kinetic energy in the free shear layer, and the latter solves the equation for turbulence frequency $\omega$ in the inner region of the boundary layer [22]. the turbulence kinetic energy $k$ and the turbulent-specific dissipation rate $\omega$ are given by the transport equations [20]:

$$\frac{\partial(\rho k)}{\partial t} + \frac{\partial}{\partial x_j}\left(\rho k \overline{u_i}\right) = \frac{\partial}{\partial x_j}\left(\mu + \frac{\mu_t}{\sigma_k}\right) + \mu_t S^2 - Y_k, \quad (4)$$

$$\frac{\partial(\rho \omega)}{\partial t} + \frac{\partial}{\partial x_j}\left(\rho \omega \overline{u_i}\right) = \frac{\partial}{\partial x_j}\left(\mu + \frac{\mu_t}{\sigma_\omega}\right) + G_\omega - Y_\omega, \quad (5)$$

Where: $\sigma_k$ and $\sigma_\omega$ are the turbulent Prandtl number for $k$ and $\omega$ respectively; $\mu_t$ is the turbulent viscosity; $\mu_t S^2$ and $G_\omega$ represent the generation of $k$ and $\omega$ respectively ; $Y_k$ and $Y_\omega$ represent the dissipation of $k$ and $\omega$ respectively ; $S$ is the modulus of mean strain-rate tensor.

the model was adopted owing to the high curvature of the impeller blade and the ability of the model to perform well in flows exhibiting adverse pressure gradients. The finite volume method (FVM) is used to discretize the transport equations of continuity, momentum, and turbulence quantities in the computational domain. A Second-order high-resolution discretization scheme is selected for both turbulent kinetic energy and turbulent specific dissipation rate. The coupled algorithm was used for the pressure–velocity coupling in the steady state calculations, whereas the segregated algorithm SIMPLEC was selected in the unsteady calculation. Second order upwind discretization was used for convection terms and central differencing schemes for diffusion terms. For the unsteady simulation, the second-order implicit scheme was applied to discretize the time-dependent terms.

### 3.3. Unsteady solution control

Due to the large number of nodes employed, the SIMPLEC algorithm was used for the pressure-velocity coupling to achieve solution convergence, a small-time step size was chosen properly to ensure numerical stability and get sufficient time to resolve the unsteady interactions of the rotating blades, and the casing walls. For this case a complete impeller revolution is performed every 720 steps, therefore the time step size that is related to the rotational speed imposed is equal to $\Delta t = T/720 = 8.46024 \times 10^{-05}$ . this time step size corresponds to a rotation of 0.5° of the impeller. The number of iterations at every time step is adjusted to reduce the residuals to the value of $10^{-6}$ for the continuity and $10^{-7}$ for the momentum and turbulence quantities. Over 45 iterations at each time step were required to achieve the final residual level.

### 3.4. Meshing procedure and sensitivity

The discretization of the computational domain was performed using ANSYS ICEM-CFD software. Because of the complexity of the computational domain and the high curvature of the impeller blade, unstructured tetrahedral mesh was used for mesh resolution in the core region of the fan domain. Non conformal mesh interfaces were used to permit flux to pass from different cell zone boundaries of the rotating and stationary domains during unsteady calculation. in such sliding interfaces, the interface cell's face need not be identical. In order to achieve grid independent solution, the required number of cells was judged by the trend of the power shaft $W_{shaft}$ as a mesh independent solution indicator in a steady state simulation at a fixed blade pitch position and at the design flow rate $Q_d$. The numerical results obtained from coarse to dense mesh are listed in Table 2. It is noteworthy that mesh refinement should not include all the cell zones of the computational domain and regions of different parts of the centrifugal fan. Therefore, successive mesh density refinement focused only on the blade surface, the blade passage within the impeller region, and the casing throat region with a smooth transition from low to high grid density region. A sectional view of the mesh of the whole fan is shown in Fig. 3.

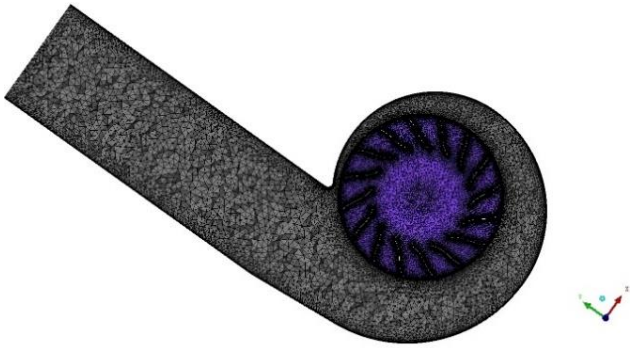

Fig. 3 Cut plane of the mesh normal to the Z-axis

As can be noted from Table 2, the numerical results become unaffected by the grid refinement when the grid number is more than 5.57 million, to reduce the computational burden, the total number of nodes retained for a mesh-independent solution for this simulation included 5574675 of unstructured tetrahedral cells. In order to meet the mesh resolution requirement of the SST k-ω model, several simulations at each operating condition were conducted to adjust the first layer height of the prism mesh normal to the wall region in different boundary walls, the non-dimensional wall distance of the first layer $y^+$ in the mesh should satisfy the condition that $y^+ \leq 1$.

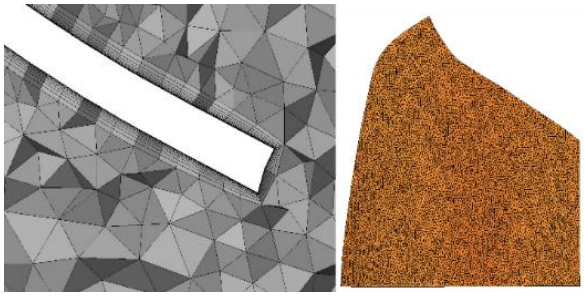

Fig. 4 Mesh resolution on the blade surface and in the near-wall region of the leading edge

Fig. 4 shows the fine mesh on the near-wall region and on the blade surface for the numerical simulation with a total of 12 prism layers normal to the wall to resolve the boundary layer. The mesh scheme employed at each flow condition was sufficient to get the value of $y^+$ within the recommended bound with a maximum value of 5 on all of the impeller surfaces. Different grid quality statistics skewness, aspect ratio, orthogonal quality, and the total number of nodes for the three cell zones of the computational domain are listed in Table 3.

Table 2

Grid density sensitivity of $W_{shaft}$

| Number of nodes (million) | 4.3 | 5.1 | 5.57 | 5.58 | 5.98 |
|---|---|---|---|---|---|
| $W_{shaft}$, kW | 495.3 | 492.1 | 488.4 | 488.1 | 487.9 |

Table 3

Number and quality statistics of the grid

| Zones | total nodes | | Skew | Aspect ratio | Orthogonal quality |
|---|---|---|---|---|---|
| Impeller | 4806381 | Min | 0.33 | 2 | 0.13 |
| | | Max | 1 | 21.99 | 1 |
| | | Average | 0.94 | 4.37 | 0.77 |
| Casing | 748484 | Min | 0.4 | 2 | 0.31 |
| | | Max | 1 | 10.28 | 1 |
| | | Average | 0.94 | 4.31 | 0.778 |
| Cone inlet | 19810 | Min | 0.71 | 2 | 0.201 |
| | | Max | 0.99 | 17.016 | 0.99 |
| | | Average | 0.93 | 4.39 | 0.769 |

### 3.5. Boundary conditions

Boundary conditions for fan simulation can be modeled using two methods. The first method consists of fixing a volume flow rate by providing a velocity profile at the fan intake and static pressure at the outlet, then varying the velocity profile for each flow rate.in the second method, the total pressure at the inlet and the pressure drop at the outflow are both specified. Since the flow rate is not known before the calculation the pressure drop is then altered to simulate it. In this study, as the first approach converges more quickly than the second approach in this simulation, it was used to implement the boundary conditions. A straight section upstream of the inlet with an extension of twice the diameter of the inlet cone was added to give the inflow more length to develop. Similarly, to avoid reverse flow at the fan outlet, the outlet section of the casing was extended four times the hydraulic diameter of the casing duct. Four flow rates were considered in the simulation namely, the design volume flow rate $Q_d$ (53.9 m$^3$/s) corresponding to the peak efficiency operating point, close to the peak pressure operating point corresponding to a volume flow rate of 48 m$^3$/s (0.89 $Q_d$), 58.82 m$^3$/s, and at a volume flow rate of 72 m$^3$/s (1.33 $Q_d$). Uniform velocity profile was imposed at the inlet section of the fan for each flow rate and atmospheric pressure was applied at the outlet section of the fan. The backflow turbulence intensity is 5% and the backflow turbulent viscosity ratio is 10. A uniform values of turbulence quantities at boundaries were used to specify turbulence parameters, Medium turbulent level was set in terms of two turbulent quantities, a turbulent intensity of 5% and a viscosity ratio of ten.no-slip boundary conditions was set to all of the wall surfaces.

## 4. Results and discussion

### 4.1. Numerical results validation

The modelling approach developed in this study is validated by comparing the numerical and experimental data of the studied centrifugal fan. The unsteady simulation results and the experimental performance curves are shown in Figs. 5 and 6. the unsteady numerical results were obtained by time-averaging the numerical quantities of the unsteady simulation over the last impeller revolution. The time periodic solutions convergence was assessed using monitored data such as the net total torque $\tau$ on the impeller. The evolution of the total torque in time during the unsteady simulation is illustrated in Figs. 7 and 8. As can be observed from the figures, that after a start-up phase, the unsteady solution starts to show periodic behavior after at least one and a half impeller revolution depending on the operating condition. Due to the fine time step and mesh employed in the case under study, each operating point took about 360 hours of calculation on a 12-core CPU and 64 GB of RAM. The fan total pressure is calculated by the difference between the mass-weighted averaged total pressure at the casing outlet and the impeller inlet. The fan efficiency was calculated based on the equation:

$$\eta_{total} = \frac{Q\Delta p_{tot} T}{\tau 2\pi}, \tag{6}$$

where: $\tau$ is the total torque obtained by integrating the total moment along the direction of the axis of rotation (Z-axis) of both the pressure and friction forces on all the impeller wall surfaces; $Q$ is the flow rate; $T$ is the impeller period; $\Delta p_{tot}$ is the total pressure rise.

According to Figs. 5 and 6, The numerical results obtained from the unsteady simulation follow the trend of the experimental performance curve with an acceptable deviation, this indicates that the modelling approach adopted is valid for predicting the flow field in the centrifugal fan. The time-averaged total pressure rise was under-predicted by a maximum value of 2.55% for a flow rate of 0.89 $Q_d$, and by 0.39% for the design operating point. Whereas, the power shaft was over-predicted by a maximum value of 3.81% for a flow rate of 1.33 $Q_d$. Fig. 5 indicates that the predicted power output $W_{shaft}$ deviation correlates with the flow rate. The numerical method was able to predict the net torque on the impeller with an error of less than 3% on average. The over prediction of the net torque is caused by some large oscillations as shown in Fig. 8.

Table 4

Calculated power shaft with the MRF approach

| Flow ratesm m$^3$/s | 48 | 53.9 | 58.82 | 72 |
|---|---|---|---|---|
| $W_{shaft}$, kW | 423.64 | 488.4 | 502.88 | 566.523 |
| Relative error, % | 7.25 | 13.58 | 10.52 | 7.9 |

It is worth noting that the discrepancy between the power shaft calculated by the frozen-rotor simulation and experiment data is much higher as compared with the results obtained from the sliding mesh approach. Table 4 shows the power shaft obtained from the steady simulation using the MRF approach.

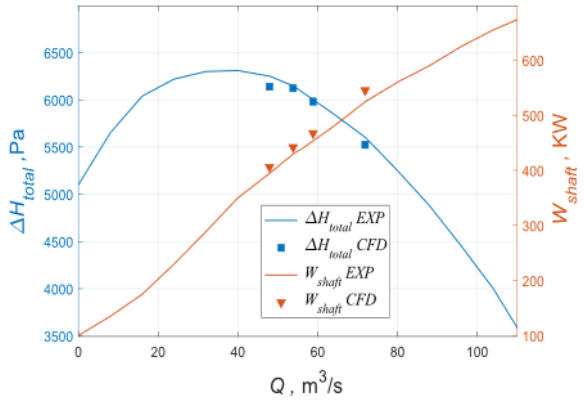


Fig. 5 Numerical validation with the characteristic curve of the studied fan ($\Delta H_{total}$ - $Q$, $W_{shaft}$ - $Q$)

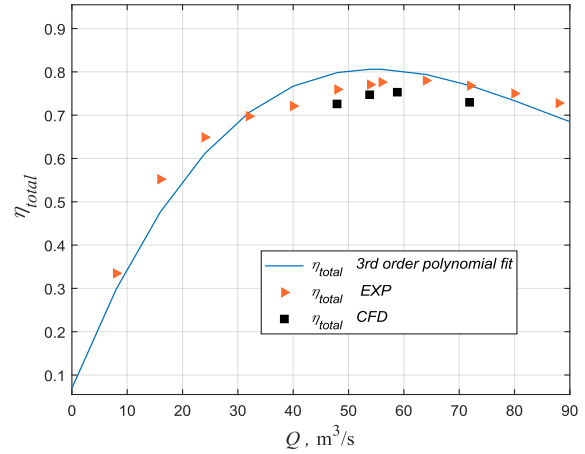


Fig. 6 Numerical validation with the characteristic curve of the studied fan ($\eta_{total}$ -$Q$)

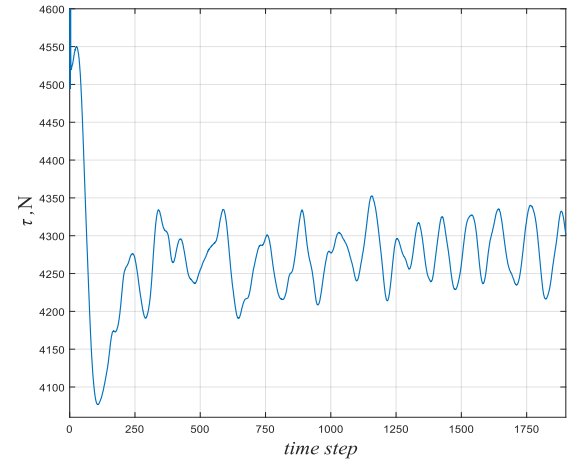


Fig. 7 Evolution of torque in time at $Q_d$

According to Table 4, the power output was over-predicted by a maximum value of 13.58% at $Q_d$, and by 9.81% on average. This indicates that the flow-field within the blade passage was not calculated properly. While the primary disadvantage of using the sliding mesh technique is the increase of computational power that is required to account for the rotor-stator coupling, the simplification of the flow physics provides an insight into the numerical accuracy limitations when using frozen-rotor simulation to predict the overall fan performance, this leads to a conclusion that the steady simulation (MRF approach) is not reliable and insufficient during the test of typical large-sized centrifugal fan, particularly when the rotor-stator interactions are important, and therefore only the unsteady numerical method is capable of providing an accurate prediction of the aerodynamic performance within an acceptable error.

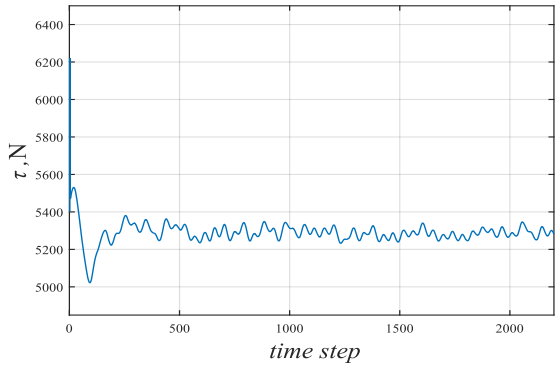


Fig. 8 Evolution of torque in time at 1.33 $Q_d$

## 4.2. Flow field analysis

### 4.2.1. Pressure field

In order to visualize the pressure distribution A cross-section plane perpendicular to the axis of rotation is defined at the middle span of the impeller ($Z_1$=0.14 m). the pressure distribution is only taken into consideration on the section $Z_1$ at the design flow rate $Q_d$ because Both time-averaged and instantaneous static pressure show nearly the same distribution at various sections of the impeller span.

Fig. 9 displays the time-averaged static pressure distribution in the section $Z_1$. The figure shows that the static pressure rises from the impeller intake to the casing outlet as the dynamic pressure generated by the impeller spinning was converted into static pressure along the casing with a high-pressure gradient in the radial direction.in the tongue tip, the static pressure reached a maximum value where the flow stagnation occurred. The static pressure in the impeller blade passage is higher on the blade pressure side than on the suction side, which gradually increases from the impeller entry to the impeller outlet. The static pressure value is lowest at the blade leading edge tip where the fluid relative velocity reaches high values therein.

The instantaneous static pressure distribution depicted in Fig. 10 shows that as the blade passes by the casing tongue, there is a comparatively higher pressure on the blade pressure side. Meanwhile, the static pressure on the blade pressure side decreases as the blade spins from the casing throat to the large discharge section of the volute, thus the non-uniformity of the pressure distribution on the blades is influenced by the geometric asymmetry of the volute.

The unsteady interaction between the impeller and the casing is assessed by the root-mean-square of static pressure field $P_{rms}$ in the section $Z_1$ at the design flow rate $Q_d$. The $P_{rms}$ distribution is shown in Fig. 11 and is given as follows:

$$p_{rms} = \sqrt{\sum_{i=1}^{n} (p_i - \overline{p})^2 / n} \,, \tag{7}$$

where: $p_i$ is the fluctuation of the static pressure over time history of one revolution; $\overline{p}$ is the time-averaged static pressure over one revolution; $n$ is the number of samples.

It is important to distinguish between the Reynolds decomposition statistical mean and the mean employed in Eq. (7). The root-mean-square is regarded as an indicator of the degree of fluctuation caused by the unsteady interaction between the impeller and the casing instead of turbulence fluctuation. The distribution of the $P_{rms}$ was higher in the impeller blade passage and in the casing throat region, as shown in Fig. 11, and it was not evenly distributed through each blade passage. Significant static pressure fluctuation values were found within the impeller blade passage, particularly on blade suction side, where the predominant flow separation and recirculation occurred, and at the blade leading edge, where the relative velocity magnitude of the flow entering the impeller is high. These significant fluctuations are more noticeable in the blade passages downstream the casing tongue where the interaction between the rotating impeller and the stationary volute is strongest. The root-mean-square of static pressure can reach a maximum value of roughly 23% of the reference pressure $p_{ref}$. The pressure distribution and the fluctuation strength on the blade passage are affected by the unsteadiness induced by these interactions, and this behavior cannot be captured by using the frozen-rotor approach.

4.2.2. Velocity and turbulent kinetic energy field

Numerical results at two different time instants were saved to show the relevance of the unsteady simulation to the impeller-volute interaction, these two-time instants are referred to $t_0$ and $t_1$ which differ by a one blade passage corresponding to 45-time steps.

The velocity field is illustrated with respect to the appropriate reference frame, so contours of relative velocity magnitude with respect to the moving reference frame for the impeller domain and the absolute velocity magnitude with respect to the inertial reference frame for the casing domain are shown in Fig. 12, a and Fig. 12, b respectively. The velocity magnitude contours with the vector field in the impeller and the casing domain in the same section $Z_1$ at the design flow rate $Q_d$ and at time instant $t_0$ *and* $t_1$ are shown in these figures. The relative velocity contours indicate the presence of flow separations on the majority of the blade-to-blade passage, and this separated flow completely dominates the impeller suction side region right after the blade leading edge. High flow velocity values are located at the leading edges and in the impeller outlet close to the blade pressure side, whereas zones associated with flow separations and the casing tongue where flow stagnation occurred have low velocity. An important factor to consider during the design phase is the blade inlet angle since it greatly affects the flow at the impeller entry and in the passage between the blades. Due to the impeller blade's curvature (as shown in Fig. 2) and improper inlet blade angle, which causes the non-alignment of the incoming flow with the impeller blade, there is flow separation in almost all of the blade passage and vortices were created right after the leading edge on the blade suction side. Due to the unsteady nature of the impeller-volute interaction, it can be seen that the flow dynamics in each blade channel at the two time instants $t_0$ and $t_1$ are different as a result of the volute's geometrical asymmetry. Additionally, the relative velocity in the outlet periphery of the blade pressure side as well as the recirculating flow are attenuated in the blade passages downstream the casing tongue due to the variation in the counter-pressure, which depends on the angular position of each blade passage relative to the volute tongue. As the blade rotates toward the large cross section of the casing, the extent of flow separation close to the blade suction side increases significantly.

The absolute velocity in the casing domain follows the same pattern, at the impeller's trailing edge, it is not uniform throughout the circumferential direction and exhibits distortion on the blade passage downstream the casing tongue. A transient simulation is required to accurately represent the unsteadiness of the flow field in the blade passage because the flow dynamics in each blade passage changes depending on the time instant and is characterized by an unsteady interaction between the impeller and the discharge volute.

The turbulent kinetic energy at section $Z_1$ shown in Fig. 12, c indicates that large turbulent kinetic energy values existed in the zones associated with flow separation where the flow is highly unstable, and in the impeller outlet discharge of the blade suction side where absolute velocity reaches maximum values, in contrast, the low turbulent kinetic energy values are located in the blade passage where the flow is radial and, in the near wall regions where the velocity gradients is high.

Based on the numerical method previously stated, the relative velocity flow field and relative streamlines within the impeller domain are compared at three flow rates: 0.89 $Q_d$ which corresponds the near peak pressure flow rate, the design flow rate $Q_d$ and 1.33 $Q_d$.

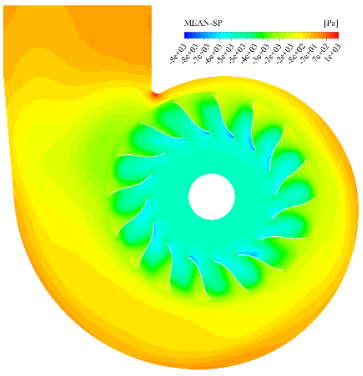


Fig. 9 Time-averaged static pressure on section $Z_1$ at $Q_d$

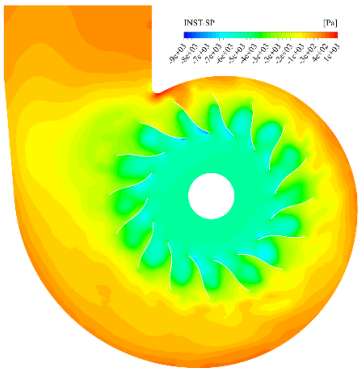


Fig. 10 Instantaneous static pressure on section $Z_1$ at $Q_d$

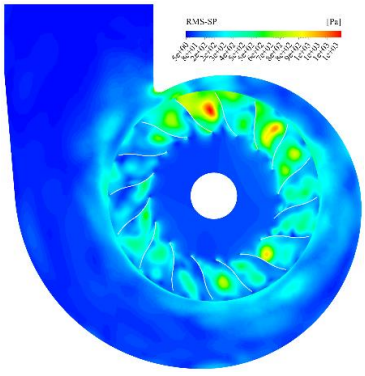


Fig. 11 $P_{rms}$ distribution on section $Z_1$ at $Q_d$

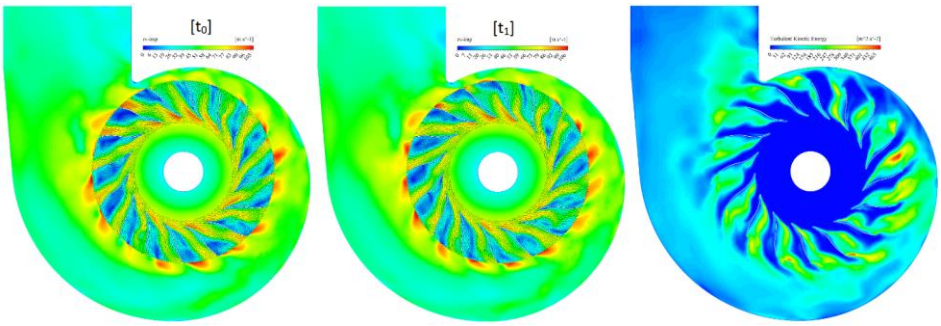


a b c

Fig. 12 Velocity and turbulent kinetic energy field on the section $Z_1$ and at $Q_d$ : a) velocity field at $t_0$; b) velocity field at $t_1$; c) turbulent kinetic energy

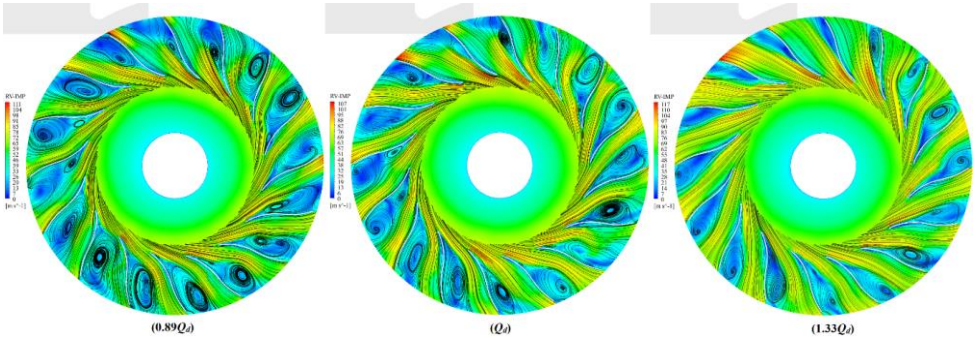


a b c

Fig. 13 Cross section of relative velocity and streamlines on the section $Z_1$: a) 0.89 $Q_d$; b) $Q_d$; c) 1.33 $Q_d$

Fig. 13 shows the relative velocity magnitude and relative streamlines on section $Z_1$ for the three operating conditions. For the three working conditions, the fluid dynamics in the blade passage were essentially, with the flow in the impeller inlet having a radial direction. Separated flow is present on almost of the blade passage with small extension in the blade passages downstream the volute tongue which is clearly apparent at the flow rate of 1.33 $Q_d$. The relative velocity streamlines indicate the presence of double separation just after the leading edge of the blade suction side in some blade-to-blade passage at $Q_d$ and 0.89 $Q_d$ of flow rate.in contrast, the fan flow-field at 1.33 $Q_d$ of flow rate is associated with one separation in the passage near the blade suction side.

## 5. Conclusion

The reported research in this paper presents the validation of a numerical approach regarding the prediction of the overall performance of a large-sized centrifugal fan installed in a cement factory. A fully resolved sliding mesh approach was conducted in the whole three-dimensional domain of the fan to take into account the unsteady interaction between the impeller and the casing. Despite the use of a URANS simulation, the numerical approach predicted the total pressure rises and the power output within a reasonable error. The unsteady simulation adopted under-predicted the total pressure rise by a maximum of 2.55%, and over predicted the power output by 3.81%. The steady MRF approach, on the other hand, over predicted the power output by 9.81% in average, which shows that the flow-field within the impeller passage was not properly resolved even at design working condition. This accuracy limitation stems from the simplification that consists of neglecting the unsteady interaction between the impeller and the volute. The examination of the flow-field reveals that there are inevitable flow separation regions in the blade passage, particularly on the blade suction side right after the leading-edge tip. This work will be extended in a further study by using the flow field solution obtained as a continuous phase to examine the erosion behavior in the fan.

## References

1. **Cardillo, L.; Corsini, A.; Delibra, G.** et al. 2014. Simulation of particle-laden flows in a large centrifugal fan for erosion prediction, Proceedings of the ASME Turbo Expo 1A. https://doi.org/10.1115/GT2014-25865.
2. **Cardillo, L.; Corsini, A.; Delibra, G.** et al. 2014. Predicting the performance of an industrial centrifugal fan incorporating cambered plate impeller blades, Periodica Polytechnica Mechanical Engineering 58(1): 15-25. https://doi.org/10.3311/PPme.7397.
3. **Aldi, N.; Casari, N.; Pinelli, M.** et al. 2019 Erosion behavior on a large-sized centrifugal fan, 13th European Turbomachinery Conference on Turbomachinery Fluid Dynamics and Thermodynamics, ETC 2019: 1-13. https://doi.org/10.29008/etc2019-389.
4. **Zhang, J.; Han, Z.; Yin, W.** et al. 2013. Numerical experiment of the solid particle erosion of bionic configuration blade of centrifugal fan, Acta Metallurgica Sinica (English Letters) 26(1): 16-24. https://doi.org/10.1007/s40195-012-0058-8.
5. **Song, X.; Qi, D.; Xu, L.** et al. 2021. Numerical simulation prediction of erosion characteristics in a double-suction centrifugal pump, Processes 9. https://doi.org/10.3390/pr9091483.

6. **Ghenaiet, A.** 2021. Study of particle dynamics and erosion in a centrifugal fan, 14th European Conference on Turbomachinery Fluid Dynamics and Thermodynamics, ETC 1-12. https://doi.org/10.29008/etc2021-495.
7. **Lai, F.; Wang, Y.; Ei-Shahat, S. A.** et al. 2019. Numerical study of solid particle erosion in a centrifugal pump for liquid-solid flow, Journal of Fluids Engineering, Transactions of the ASME 141(12). https://doi.org/10.1115/1.4043580.
8. **Zhao, R. J.; Zhao, Y. L.; Zhang, D. S.** et al. 2021. Numerical investigation of the characteristics of erosion in a centrifugal pump for transporting dilute particle-laden flows, Journal of Marine Science and Engineering 9(9). https://doi.org/10.3390/jmse9090961.
9. **Huang, S.; Su, X.; Qiu, G.** 2015. Transient numerical simulation for solid-liquid flow in a centrifugal pump by DEM-CFD coupling, Engineering Applications of Computational Fluid Mechanics 9: 411-418. https://doi.org/10.1080/19942060.2015.1048619.
10. **Ballesteros-Tajadura, R.; Velarde-Suárez, S.; Hurtado-Cruz . J. P.; Santolaria-Morros, C.** 2006. Numerical calculation of pressure fluctuations in the volute of a centrifugal fan, Journal of Fluids Engineering, Transactions of the ASME 128: 359-369. https://doi.org/10.1115/1.2170121.
11. **Pritz, B.; Probst, M.; Wiśniewski, P.** et al. 2021. Identification of unsteady effects in the flow through a centrifugal fan using CFD/CAA methods, 42: 169-181. https://doi.org/10.24425/ather.2021.139657.
12. **Zhang, N.; Liu, X.; Gao, B.; Xia, B.** 2019. DDES analysis of the unsteady wake flow and its evolution of a centrifugal pump, Renewable Energy 141: 570-582. https://doi.org/10.1016/j.renene.2019.04.023.
13. **Cai, J. C.; Chen, H. J.; Brazhenko, V.; Gu, Y. H.** 2021. Study of the hydrodynamic unsteady flow inside a centrifugal fan and its downstream pipe using detached eddy simulation, Sustainability (Switzerland) 13(9). https://doi.org/10.3390/su13095113.
14. **Zhang, N.; Jiang, J.; Gao, B.** et al. 2020. Numerical analysis of the vortical structure and its unsteady evolution of a centrifugal pump, Renewable Energy 155: 748-760. https://doi.org/10.1016/j.renene.2020.03.182.
15. **Younsi, M.; Bakir, F.; Kouidri, S.; Rey, R.** 2007. Numerical and experimental study of unsteady flow in a centrifugal fan, Proceedings of the Institution of Mechanical Engineers, Part A: Journal of Power and Energy 221:1025-1036. https://doi.org/10.1243/09576509JPE445.
16. **Yang, J.; Meng, L.; Zhou, L.;** et al. 2013. Unsteady internal flow field simulations in a double suction centrifugal fan, Engineering Computations 30: 345-356. https://doi.org/10.1108/02644401311314321.
17. **Peng, G.; Hong, S.; Chang, H.** et al. 2022. Numerical and experimental research on the influence of clearance between impeller and cover on the pump performance, Mechanika 28: 67-72. https://doi.org/10.5755/j02.mech.28904.
18. **Mohammadi, N.; Fakharzadeh, M.** 2017. Analysis of effect of impeller geometry including blade outlet angle on the performance of multi-pressure pumps: Simulation and experiment, Mechanika 23:107-119. https://doi.org/10.5755/j01.mech.23.1.17676.
19. Industrial Fans Performance Testing using Standardized Airways. ISO 5801.2007.
20. Ansys Fluent Theory Guide. 2020 R1. [accessed January. 2020]. Available from Internet: https://www.ansys.com.
21. **Corsini, A.; Delibra, G.; Sheard, A. G.** 2013. A critical review of computational methods and their application in industrial fan design, ISRN Mechanical Engineering 2013(327). https://doi.org/10.1155/2013/625175.
22. **Menter, F. R.** 1994. Two-equation eddy-viscosity turbulence models for engineering applications, AIAA Journal 32(8):1598-1605. https://doi.org/10.2514/3.12149.

A. Amour, N. Menasri

TRANSIENT NUMERICAL SIMULATION OF A LARGE-SIZED CEMENT-MILL FAN FOR PERFORMANCE PREDICTION

S u m m a r y

In many engineering applications, particle-laden flows are a necessary part of the conveying process, but in other situations, they could have unintended consequences that must be avoided. As a part of the exhausting process, the induced cement-mill fan (FN-280) installed in a cement plant operates under critical conditions with the presence of high content of cement particles. Over time the dragged solid particles erode the rotating and stationary parts of the fan causing their damage. If one decides on a numerical approach to predict regions most prone to erosion and track the solid particle's trajectory within the fan domain by assuming a one-way coupling regime between the continuous and discrete solid phases, a deep insight into the flows physics within the centrifugal fan is required. With this aim, a three-dimensional numerical approach for the hole unsteady flow in a large-sized industrial centrifugal fan has been carried out in this paper. A fully resolved sliding mesh approach was employed to take into account the unsteady interaction between the impeller and the discharge volute. Based on the characteristic performance curves, the numerical results of the unsteady simulation at four operating conditions are validated with the experimental data. The comparisons reveal that the results of the unsteady simulation are in an acceptable level of agreement with the experiment, demonstrating the validity of the modelling approach adopted in this study.

**Keywords:** CFD, centrifugal fan, fan performance, induced draft fan, sliding mesh technique.

Received August 28, 2022
Accepted January 27, 2023

This article is an Open Access article distributed under the terms and conditions of the Creative Commons Attribution 4.0 (CC BY 4.0) License (http://creativecommons.org/licenses/by/4.0/).